

An optically-selected cluster catalog at redshift $0.1 < z < 1.1$ from the Hyper Suprime-Cam Subaru Strategic Program S16A data

Masamune OGURI^{1,2,3}, Yen-Ting LIN⁴, Sheng-Chieh LIN^{4,5},
Atsushi J. NISHIZAWA^{6,7}, Anupreeta MORE³, Surhud MORE³,
Bau-Ching HSIEH⁴, Elinor MEDEZINSKI⁸, Hironao MIYATAKE^{9,3},
Hung-Yu JIAN⁴, Lihwai LIN⁴, Masahiro TAKADA³, Nobuhiro OKABE^{10,11},
Joshua S. SPEAGLE^{12,3}, Jean COUPON¹³, Alexie LEAUTHAUD^{14,3},
Robert H. LUPTON⁸, Satoshi MIYAZAKI^{15,16}, Paul A. PRICE⁸,
Masayuki TANAKA¹⁵, I-Non CHIU⁴, Yutaka KOMIYAMA^{15,16},
Yuki OKURA^{17,18}, Manobu M. TANAKA¹⁹ and Tomonori USUDA^{15,16}

¹Research Center for the Early Universe, University of Tokyo, Tokyo 113-0033, Japan

²Department of Physics, University of Tokyo, Tokyo 113-0033, Japan

³Kavli Institute for the Physics and Mathematics of the Universe (Kavli IPMU, WPI), University of Tokyo, Chiba 277-8582, Japan

⁴Institute of Astronomy and Astrophysics, Academia Sinica, P.O. Box 23-141, Taipei 10617, Taiwan

⁵Department of Physics, National Taiwan University, 10617 Taipei, Taiwan

⁶Institute for Advanced Research, Nagoya University, Aichi 464-8601, Japan

⁷Department of physics, Nagoya University, Aichi 464-8602, Japan

⁸Department of Astrophysical Sciences, Princeton University, Princeton, NJ 08544, USA

⁹Jet Propulsion Laboratory, California Institute of Technology, Pasadena, CA 91109, USA

¹⁰Department of Physical Science, Hiroshima University, 1-3-1 Kagamiyama, Higashi-Hiroshima, Hiroshima 739-8526, Japan

¹¹Hiroshima Astrophysical Science Center, Hiroshima University, Higashi-Hiroshima, 1-3-1 Kagamiyama 739-8526, Japan

¹²Department of Astronomy, Harvard University, Cambridge, MA 02138, USA

¹³Astronomical Observatory of the University of Geneva, ch. d'Ecogia 16, CH-1290 Versoix, Switzerland

¹⁴Department of Astronomy and Astrophysics, University of California Santa Cruz, Santa Cruz, CA 95064, USA

¹⁵National Astronomical Observatory of Japan, Mitaka, Tokyo 181-8588, Japan

¹⁶Department of Astronomy, School of Science, Graduate University for Advanced Studies, Mitaka, Tokyo 181-8588, Japan

¹⁷RIKEN Nishina Center, 2-1 Hirosawa, Wako, Saitama 351-0198, Japan

¹⁸RIKEN-BNL Research Center, Department of Physics, Brookhaven National Laboratory, Bldg. 510, Upton, NY, 11792, USA

¹⁹High Energy Accelerator Research Organization (KEK), Institute of Particle and Nuclear

Studies, 1-1 Oho, Tsukuba 305-0801

*E-mail: masamune.oguri@ipmu.jp

Received ; Accepted

Abstract

We present an optically-selected cluster catalog from the Hyper Suprime-Cam (HSC) Subaru Strategic Program. The HSC images are sufficiently deep to detect cluster member galaxies down to $M_* \sim 10^{10.2} M_\odot$ even at $z \sim 1$, allowing a reliable cluster detection at such high redshifts. We apply the CAMIRA algorithm to the HSC Wide S16A dataset covering $\sim 232 \text{ deg}^2$ to construct a catalog of 1921 clusters at redshift $0.1 < z < 1.1$ and richness $\hat{N}_{\text{mem}} > 15$ that roughly corresponds to $M_{200\text{m}} \gtrsim 10^{14} h^{-1} M_\odot$. We confirm good cluster photometric redshift performance, with the bias and scatter in $\Delta z / (1 + z)$ being better than 0.005 and 0.01 over most of the redshift range, respectively. We compare our cluster catalog with large X-ray cluster catalogs from XXL and XMM-LSS surveys and find good correlation between richness and X-ray properties. We also study the miscentering effect from the distribution of offsets between optical and X-ray cluster centers. We confirm the high (> 0.9) completeness and purity for high mass clusters by analyzing mock galaxy catalogs.

Key words: galaxies: clusters: general

1 Introduction

Clusters of galaxies are dominated by dark matter, which makes them a useful site for cosmological studies. For example, the abundance of massive clusters and its time evolution, which can well be predicted by N -body simulations, are known to be a sensitive probe of cosmological parameters (e.g., Allen et al. 2011; Weinberg et al. 2013). Detailed studies of dark matter distributions in clusters basically support the so-called cold dark matter paradigm at the non-linear scale (e.g., Oguri et al. 2010, 2012; Okabe et al. 2010, 2013; Umetsu et al. 2011, 2016; Niikura et al. 2015). In addition, clusters of galaxies play an essential role in understanding galaxy formation physics given a possible large environmental effect on galaxy formation and evolution (e.g., Renzini 2006; Kravtsov & Borgani 2012).

Clusters can be identified in various wavelengths, including optical, X-ray, and radio/mm/submm via the Sunyaev-Zel'dovich (SZ; Sunyaev & Zeldovich 1972) effect. While there are advantages and disadvantages for each method, the recent development of wide-field optical imaging surveys makes surveys of clusters in optical particularly powerful, because they take wide-field images with multi-bands, which is crucial both in selecting clusters of galaxies efficiently from the enhancement of galaxy number densities as well as deriving photometric redshifts of clusters (e.g., Gladders & Yee 2000). Indeed, large samples of optically-selected clusters have been constructed in Sloan Digital Sky Survey (Koester et al. 2007; Hao et al. 2010; Szabo et al. 2011; Wen et al. 2012; Rykoff et al. 2014; Oguri 2014), the Red-Sequence Cluster Survey (Gladders & Yee 2005), the Canada-France-Hawaii-Telescope

Legacy Survey (Milkeraitis et al. 2010; Ford et al. 2014; Licitra et al. 2016), the Blanco Cosmology Survey (Bleem et al. 2015), and the Dark Energy Survey Science Verification Data (DES; Rykoff et al. 2016). Because of the depth and wavelength coverage of these optical surveys, the redshift range of most of these clusters are restricted to $z \lesssim 0.9$ at most. Attempts to find clusters at higher redshifts have also been made using infrared data, although with generally smaller area (e.g., Goto et al. 2008; Wilson et al. 2009; Andreon et al. 2009; Gettings et al. 2012; Rettura et al. 2014).

The Hyper Suprime-Cam (HSC; Miyazaki et al. 2012, 2015) is a new wide-field optical imager installed on the Subaru 8.2-meter telescope. The HSC Subaru Strategic Program (hereafter the HSC Survey) is an ongoing wide-field optical imaging survey (Aihara et al. 2017). It consists of three layers (Wide, Deep, and Ultradeep), and the Wide layer is planned to observe the total sky area of $\sim 1400 \text{ deg}^2$ with five broadband filters (*grizy*). With its unique combination of area and depth ($i_{\text{lim}} \sim 26$ at 5σ), the HSC Wide layer is expected to revolutionize the optically-selected cluster search by constructing a large sample of massive clusters at $z \sim 1$ and beyond.

In this paper, we construct a new optically-selected cluster catalog from the first two years of observation of the HSC Survey, using the CAMIRA (Cluster finding Algorithm based on Multi-band Identification of Red-sequence gAlaxies) algorithm (Oguri 2014). We construct a catalog of 1921 clusters with richness $\hat{N}_{\text{mem}} > 15$ and the redshift range $0.1 < z < 1.1$. The catalog is compared with spectroscopic and X-ray data as well as mock galaxy catalogs to check its validity.

This paper is organized as follows. In Section 2 we describe the HSC data and the cluster finding algorithm used in the paper. Section 3 presents the cluster catalog and discusses the accuracy of photometric redshifts of the clusters. We compare the HSC cluster catalog with the SDSS CAMIRA cluster catalog in Section 4, and X-ray cluster catalogs in Section 5. We present an analysis of mock galaxy catalogs in Section 6. We summarize our results in Section 7. Throughout the paper we assume a flat Λ -dominated cold dark matter model with $\Omega_M = 0.28$, $\Omega_\Lambda = 0.72$, $h = 0.7$, $\Omega_b = 0.044$, $n_s = 0.96$, and $\sigma_8 = 0.82$. Magnitudes in this paper are in the AB magnitude system, and are corrected for Galactic extinction (Schlegel et al. 1998).

2 Data and Method

2.1 HSC Wide Data

In this paper we use the S16A internal data release of the HSC Survey, which was released in 2016 August. The S16A release contains imaging data taken between 2014 March and 2016 April, containing 174 deg² of the HSC Wide data taken in all five broadbands at full depth. The area that covers all five broadbands but with non full depth exceeds 200 deg². The HSC data are reduced with the HSC Pipeline, hscPipe (Bosch et al. 2017), which is based on the Large Synoptic Survey Telescope pipeline (Ivezic et al. 2008; Axelrod et al. 2010; Jurić et al. 2015). The Pan-STARRS1 data (Tonry et al. 2012; Schlafly et al. 2012; Magnier et al. 2013) are also used for astrometric and photometric calibrations.

We create an input galaxy catalog from the HSC database. We select galaxies that were observed in all five broadbands, by imposing cuts in the number of visits for each object using `countinputs` parameter, which indicates the number of images used to create a coadd image for each galaxy. Specifically we set `countinputs` ≥ 2 for *gr*-bands and `countinputs` ≥ 4 for *izy*-bands. While this condition is a more relaxed condition than the nominal definition of the full depth for the HSC Wide Survey (`countinputs` = 4 for *gr*-bands and `countinputs` = 6 for *izy*-bands), we adopt this condition to avoid gaps in the galaxy distribution due to CCD gaps. We only use galaxies with *z*-band `cmodel` magnitude brighter than $z = 24$, its error smaller than 0.1, and *i*-band star-galaxy separation parameter `classification_extendedness` = 1. We use *z*-band for the detection magnitude, rather than *i*-band as used in the SDSS CAMIRA cluster catalog, as it is better suited for galaxies at redshift around unity. The limiting magnitude of $z = 24$ corresponds to more than 10σ detection significance for most of the area of interest, and hence the detection completeness is very close to unity. On the other hand, we use *i*-band star-galaxy separation because *i*-band images are on average taken in better seeing conditions with a median seeing size of $\sim 0''.6$ than the other bands, in order to allow accurate galaxy shape

measurements for weak lensing analysis. In addition we place weak constraints on *ri*-bands as $r < 26.5$ and $i < 26$ mainly to remove artifacts. We also remove galaxies that can be affected by bad pixels or have poor photometric measurements, by rejecting objects with any of the following flags in any five broadbands; `flags_pixel_edge`, `flags_pixel_cr_center`, `flags_pixel_interpolated_center`, `cmodel_flux_flags`, and `parent_flux_convolved_2_0_flags`. In addition we remove objects with the flag `centroid_sdss_flags` in *riz*-bands (Aihara et al. 2017)

We use `cmodel` magnitudes, which are magnitudes derived from light profile fitting, as “total” magnitudes of galaxies (Bosch et al. 2017). However, we find that photometry with the current version of hscPipe can be inaccurate in crowded regions such as cluster centers because of failure of the deblender in such regions. More specifically, although hscPipe successfully deblends galaxies in crowded regions, magnitudes of deblended galaxies in highly crowded regions are sometimes offset significantly. Given the critical importance of accurate colors for cluster finding, in this paper we adopt the following hybrid approach for galaxy photometry. We derive colors of individual galaxies using aperture photometry on the ‘parent’ (i.e., undeblended) image after the Point Spread Function (PSF) sizes are matched between five broadbands, because this aperture photometry provide accurate colors even for galaxies in crowded regions. We use the target PSF size of $1.''1$ and the aperture size of $1.''1$ in diameter (`parent_mag_convolved_2_0`). As stated above, we use `cmodel` magnitudes, which are galaxy magnitudes from light profile fitting, for total *z*-band magnitudes, and derive magnitudes in the other bands using the colors from the aperture photometry on PSF-matched images as described above in detail.

The HSC database also provides a bright star mask. Masked areas are dependent on magnitudes of stars, and are chosen conservatively. As a result, about 10% of the area fall in the bright star mask. Here we do not apply the bright star mask to create our cluster catalog, although we also provide an HSC Wide cluster catalog constructed with the bright star mask in Appendix 1. The current version of the bright star mask contains an issue that affects cluster finding at low redshifts, which is discussed in Appendix 2. The input galaxy catalog contains 19,060,802 galaxies.

2.2 Spectroscopic Data

As discussed in Oguri (2014), we need a calibration of red-sequence galaxy colors with spectroscopic galaxies in order to improve the accuracy of our algorithm. In fact, the HSC Survey overlaps with a number of spectroscopic surveys including SDSS DR12 (Alam et al. 2015), DEEP2 DR4 (Newman et al. 2013), PRIMUS DR1 (Coil et al. 2011), VIPERS PDR1 (Garilli et al. 2014), VVDS (Le Fèvre et al. 2013), GAMA DR2

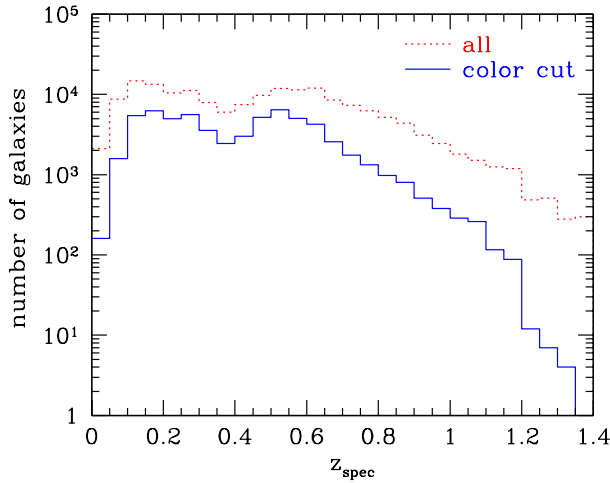


Fig. 1. The number distribution of spectroscopic galaxies in the HSC Wide Survey as a function of spectroscopic redshift. The dotted line shows the distribution for all the spectroscopic galaxies. The solid line shows the distribution after the color cuts to select red-sequence galaxies (see the text for details).

(Liske et al. 2015), WiggleZ DR1 (Drinkwater et al. 2010), zCOSMOS DR3 (Lilly et al. 2009), UDSz (Bradshaw et al. 2013; McLure et al. 2013), 3D-HST v4.1.5 (Momcheva et al. 2016), and FMOS-COSMOS v1.0 (Silverman et al. 2015). We use these spectroscopic data for the calibration.

First we cross match the spectroscopic catalogs with the HSC Wide S16A galaxy catalog constructed in Section 2.1 to obtain a sample of 171,255 galaxies with spectroscopic redshifts between $z = 0.01$ and 1.4 and the redshift error smaller than 0.01. Since we are interested in red-sequence galaxies only, we apply additional color cuts to remove obvious blue galaxies and to select galaxies used for the calibration of the red-sequence colors. Specifically we adopt the following color cuts

$$g - r > \begin{cases} 0.398 + 2.9z_{\text{spec}} & (z_{\text{spec}} \leq 0.38), \\ 1.861 - 0.95z_{\text{spec}} & (0.38 < z_{\text{spec}}), \end{cases} \quad (1)$$

$$r - i > \begin{cases} 0.2 + 0.8z_{\text{spec}} & (z_{\text{spec}} \leq 0.369), \\ -0.169 + 1.8z_{\text{spec}} & (0.369 < z_{\text{spec}} \leq 0.75), \\ 1.481 - 0.4z_{\text{spec}} & (0.75 < z_{\text{spec}}), \end{cases} \quad (2)$$

$$r - i < 2 - 0.4z_{\text{spec}}, \quad (3)$$

$$i - z > \begin{cases} 0.122 + 0.3z_{\text{spec}} & (z_{\text{spec}} \leq 0.76), \\ -1.132 + 1.95z_{\text{spec}} & (0.76 < z_{\text{spec}} \leq 0.96), \\ 0.164 + 0.6z_{\text{spec}} & (0.96 < z_{\text{spec}}), \end{cases} \quad (4)$$

$$i - z < 0.5 + 0.5z_{\text{spec}}, \quad (5)$$

where z_{spec} denotes the spectroscopic redshift. We also restrict the i -band magnitude as $i > 17$ because bright galaxies might be saturated in the HSC images. We note that these color cuts are meant for the rough selection of red-sequence galaxies and does not need to be strict as any outliers are clipped in the course of the calibration process (see Oguri 2014). We also note that

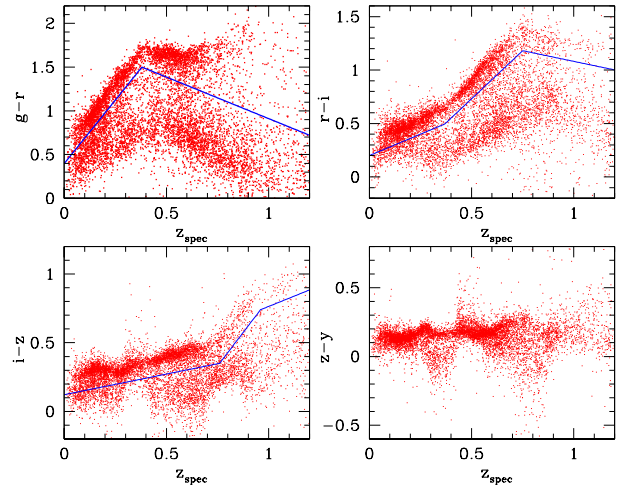


Fig. 2. Colors of spectroscopic galaxies as a function of redshift. For illustrative purpose, we plot a subsample of only 5% of all the spectroscopic galaxies. We show $g - r$ (upper left), $r - i$ (upper right), $i - z$ (lower left), and $z - y$ (lower right). Solid lines show our color cuts defined by equations (1), (2), and (4).

these color cuts are only for spectroscopic galaxies used for the calibration, i.e., we do not apply any color cuts for photometric galaxies used for cluster finding.

We show the redshift distribution of the spectroscopic galaxies for the calibration in Figure 1, and distributions of colors of the spectroscopic galaxies as well as our color cuts in Figure 2. After the color cuts the number of spectroscopic galaxies reduces to 62,998. In fact we use only 90% of the spectroscopic galaxies after the color cuts for the calibration, and reserve the remaining 10% to make sure that we are not grossly overfitting the data. To check this point, we compute photometric redshifts of individual spectroscopic galaxies using our stellar population synthesis (SPS) model with calibrated colors and derive the bias and scatter of photometric redshifts of these spectroscopic galaxies. We find that the bias and scatter are similar between spectroscopic galaxies used for the calibration and those not used for the calibration. More specifically, we compute the bias and scatter of the residual $(z_{\text{photo}} - z_{\text{spec}})/(1 + z_{\text{spec}})$ for these spectroscopic galaxies with good SPS model fitting results ($\chi^2 < 20$ for 4 degree of freedom; this cut is only for checking the accuracy of photometric redshifts for individual galaxies presented in this subsection, and in cluster finding we do not apply this χ^2 cut), and find the bias and scatter of -0.0017 and 0.021 for galaxies used for the calibration, and -0.0020 and 0.021 for galaxies not used for the calibration.

2.3 Updates of the CAMIRA Algorithm

The detailed methodology of the CAMIRA algorithm was presented in Oguri (2014). In short, it fits all photometric galaxies with a SPS model of Bruzual & Charlot (2003) to

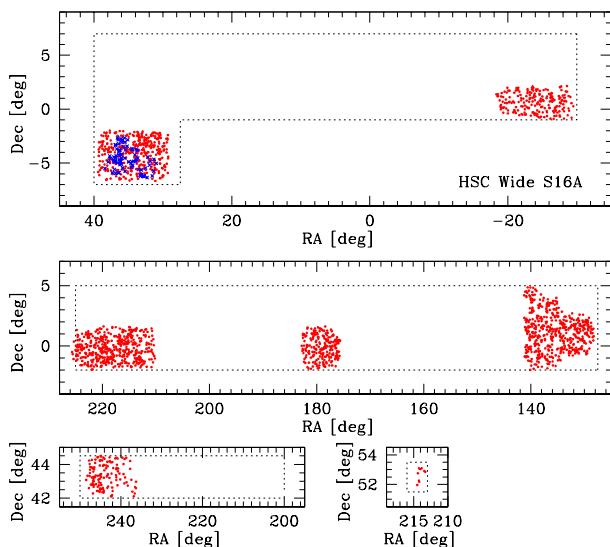


Fig. 3. Spatial distribution of clusters. Filled points show the positions of HSC Wide S16A clusters presented in this paper. The planned footprint of the entire HSC Wide Survey is the region enclosed by dotted lines. We also show the spatial distribution of X-ray clusters used in Section 5 by crosses.

compute likelihoods of being red-sequence galaxies as a function of redshift. The model is calibrated using spectroscopic galaxies, which are used to derive residual colors of SPS model fitting as a function of wavelength and redshift (see also below). Using the likelihoods we define a non-integer “number parameter” for each galaxy as a function of redshift, such that the sum of number parameters reduces to richness. Using the number parameter, the three-dimensional richness map is constructed to locate cluster candidates from peaks in the richness map. In CAMIRA, richness describes the number of red member galaxies with stellar masses $M_* \gtrsim 10^{10.2} M_\odot$ and within a circular aperture with a radius $R \lesssim 1 h^{-1} \text{Mpc}$ in physical unit. In fact we use smooth filters for stellar masses, $F_M(M_*) \propto \exp[-(M_*/10^{13} M_\odot)^4 - (10^{10.2} M_\odot/M_*)^4]$, and for spatial distributions, $F_R(R) \propto \Gamma[4, (R/R_0)^2] - (R/R_0)^4 \exp[-(R/R_0)^2]$ with $R_0 = 0.8 h^{-1} \text{Mpc}$, to compute richness. The spatial filter is a compensated filter such that the background level is automatically subtracted in deriving richness. We then identify a Brightest Cluster Galaxy (BCG) for each cluster candidate by selecting a high stellar mass galaxy near the richness peak, and refine richness, cluster photometric redshift, and the BCG, iteratively. Interested readers are referred to Oguri (2014) for more information.

In this paper, we update the CAMIRA algorithm in several ways and also adjust model parameters, in order to produce better results in the HSC Survey which covers wider redshift range than the SDSS. First, while the central wavelength λ_0 used in the polynomial fitting of the residual magnitudes of the SPS model fitting (see equation 3 in Oguri 2014) was fixed to 5000\AA , here we allow it to vary as a function of redshift, because the

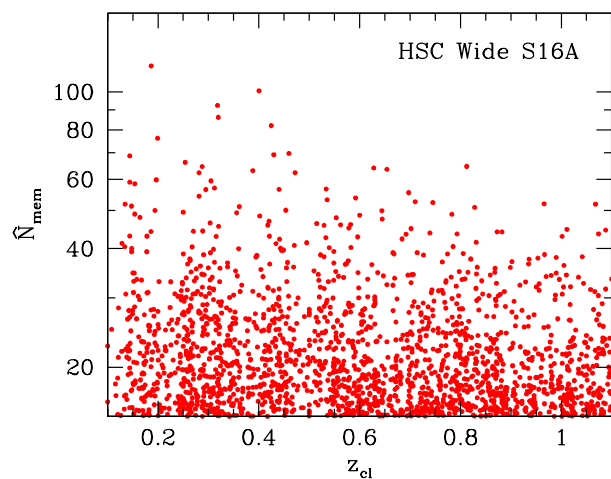


Fig. 4. Distribution of clusters in the richness-redshift plane. The cluster catalog is constructed in the redshift range $0.1 < z_{\text{cl}} < 1.1$ and the richness range $\tilde{N}_{\text{mem}} > 15$.

range of the rest frame wavelength covered by the HSC filters change significantly from $z = 0$ to $z \sim 1$. Specifically, we assume the functional form of

$$\lambda_0(z) = \lambda_{0,z=0} + \gamma z, \quad (6)$$

and adopt $\lambda_{0,z=0} = 6400 \text{\AA}$ and $\gamma = -2850 \text{\AA}$. Second, we also include the redshift dependence of the model scatter σ_{resi} . We do so by deriving σ_{resi} as a function of redshift using the spectroscopic galaxies within the redshift bin $\Delta z = 0.13$. The centering parameter σ_R in equation (19) of Oguri (2014) is modified from $\sigma_R = 0.3 h^{-1} \text{Mpc}$ to $0.12 h^{-1} \text{Mpc}$ to reduce the cluster miscentering effect (see also Section 5.4). Finally, we also update some parameters related to mask corrections, which takes account of the effect of small-scale gaps and holes seen in the input galaxy catalog (see Oguri 2014). We use new parameter values of $\theta_{\text{mask}} = 0.4$ (aperture size for creating a mask map from the input galaxy catalog), $f_{\text{mask},c} = 0.7$, and $f_{\text{mask},b} = 0.3$ (correction factors for the inner and outer parts of the spatial filter for cluster finding).

3 Cluster Catalog

3.1 Basic characteristics

We construct an HSC Wide S16A cluster catalog in the redshift range $0.1 < z_{\text{cl}} < 1.1$, where z_{cl} denotes photometric redshifts of clusters. Cluster photometric redshifts are computed in the course of CAMIRA cluster finding by combining photometric redshifts of high-confidence cluster member galaxies (see Oguri 2014). The upper limit of the redshift comes mainly from the lack of spectroscopic galaxies for the calibration, but it is also due to the limited wavelength coverage. The lower limit of the redshift is because large angular sizes of low-redshift clusters make cluster finding challenging, and member galaxies also

tend to be too bright in HSC images. We select clusters with the mask-corrected richness \hat{N}_{mem} (see Oguri 2014, for the definition) higher than $\hat{N}_{\text{mem}} = 15$. The catalog contains 1921 clusters.

In Oguri (2014), the richness \hat{N}_{mem} is further corrected for the incompleteness of detections of member galaxies. This was particularly important for SDSS in which our member galaxy selection (corresponding to $L \gtrsim 0.2L_*$) was incomplete at $z \gtrsim 0.3$ due to the shallow depth of SDSS images. In contrast, the HSC Wide Survey is deep enough to detect almost all member galaxies used for our cluster finding (including the non full-depth area we use in this paper), which again corresponds to $L \gtrsim 0.2L_*$, even at $z \sim 1.1$. Therefore in this paper we do not apply any richness correction due to member galaxy incompleteness (i.e., $\hat{N}_{\text{cor}} = \hat{N}_{\text{mem}}$ in the notation of Oguri 2014). We show the spatial distribution of the HSC Wide S16A clusters in Figure 3, and the distribution in the richness-redshift plane in Figure 4. The area of the cluster search region of HSC Wide S16A is estimated as $\sim 232 \text{ deg}^2$. The area is larger than that of the full-color and full-depth region of 174 deg^2 for the HSC Wide S16A dataset because we use the region that does not reach full depth, as described in Section 2.1. We show HSC images of the richest clusters in several different redshift ranges in Figure 5.

3.2 Number density of clusters

One way to infer the mass of a cluster catalog is to compare its number density with a number density of halos for a given cosmological model (e.g., Jimeno et al. 2017). We show the comoving number density of HSC Wide S16A clusters as a function of redshift in Figure 6. The number density declines slowly with increasing redshift, which is consistent with the DES Science Verification (SV) data redMaPPer cluster catalog (Rykoff et al. 2016) and implies the redshift evolution of the mass threshold is not strong. In order to check this point further, we compute the predicted number densities of halos with constant mass threshold using the halo mass function of Tinker et al. (2008). Here we adopt the mean overdensity mass $M_{200\text{m}}$ which is defined as the mass enclosed within a sphere of radius $r_{200\text{m}}$ within which the mean density is 200 times the mean matter density of the Universe. The comparison shown in Figure 6 suggests that our richness threshold of $\hat{N}_{\text{mem}} > 15$ roughly corresponds to the mass threshold of $M_{200\text{m}} \gtrsim 10^{14} h^{-1} M_{\odot}$.

3.3 Performance of photometric redshifts

Photometric redshifts of clusters, z_{cl} , are derived on the course of cluster finding (see Oguri 2014). In order to check the accuracy of cluster photometric redshifts, we cross-match the HSC Wide S16A cluster catalog with the spectroscopic galaxy catalog (Section 2.2). We find that BCGs of 843 clusters have

spectroscopic redshifts, $z_{\text{BCG,spec}}$. Figure 7 compares z_{cl} and $z_{\text{BCG,spec}}$, which clearly shows that cluster photometric redshifts are quite accurate for the whole redshift range. To quantify the accuracy of cluster photometric redshifts, we compute the residual $(z_{\text{cl}} - z_{\text{BCG,spec}})/(1 + z_{\text{BCG,spec}})$ for all the clusters and define the bias δ_z and scatter σ_z by average and standard deviation of the residual with 4σ clipping. We then define the outlier rate f_{out} as the fraction of galaxies that are removed by the 4σ clipping. Using all the galaxies, we find the bias $\delta_z = -0.0013$, the scatter $\sigma_z = 0.0081$, and the outlier rate $f_{\text{out}} = 0.017$. In Figure 7 we also show the bias δ_z and scatter σ_z as a function of redshift, finding that the bias is $|\delta_z| < 0.005$ and the scatter is $\sigma_z < 0.01$ for most of the redshift range. This performance of cluster photometric redshifts is comparable to that of SDSS redMaPPer and CAMIRA clusters (Rykoff et al. 2014; Oguri 2014) and better than that of DES SV redMaPPer clusters (Rykoff et al. 2016). We note that the availability of a large sample of spectroscopic galaxies from SDSS and other spectroscopic surveys (see Section 2.2) is an advantage of the HSC Survey over DES. However, as is clear from Figure 7, there are not many spectroscopic galaxies at $z \gtrsim 0.8$, which suggests the importance of spectroscopic follow-up observations of those high-redshift clusters to test their reliability further.

4 Comparison with SDSS

Since the HSC data is much deeper than SDSS, it is expected that we can identify cluster member galaxies more reliably in HSC, down to the stellar mass limit for the richness calculation, $\sim 10^{10.2} M_{\odot}$, which roughly corresponds to the luminosity range of $L \gtrsim 0.2L_*$ recommended in Rykoff et al. (2012). Due to the shallowness of the SDSS data, in Oguri (2014) we applied a richness correction factor $f_N(z) = \hat{N}_{\text{mem}}/\hat{N}_{\text{cor}}$ to account for the incompleteness of member galaxy detections. In contrast, as discussed in Section 3.1, in HSC we do not apply any correction for the member galaxy incompleteness simply because HSC data are deep enough to detect all the member galaxies of interest out to $z \sim 1.1$. Thus we compare the richness in SDSS and HSC to check the accuracy of the incompleteness correction.

We cross match the CAMIRA SDSS catalog with the HSC Wide S16A catalog. Our matching criterion is that clusters whose physical transverse distance is within $1h^{-1}\text{Mpc}$ and the difference in cluster photometric redshifts is smaller than 0.1. For the SDSS cluster catalog, we use an updated (v1.2) CAMIRA SDSS cluster catalog which slightly differs from the cluster catalog published in Oguri (2014). The updated CAMIRA SDSS catalog¹ adopts the new centering parameters described in Section 2.3, and contains 83735 clusters in the

¹ The updated CAMIRA SDSS cluster catalog (version 1.2) is available at <http://www.slac.stanford.edu/~oguri/cluster/>.

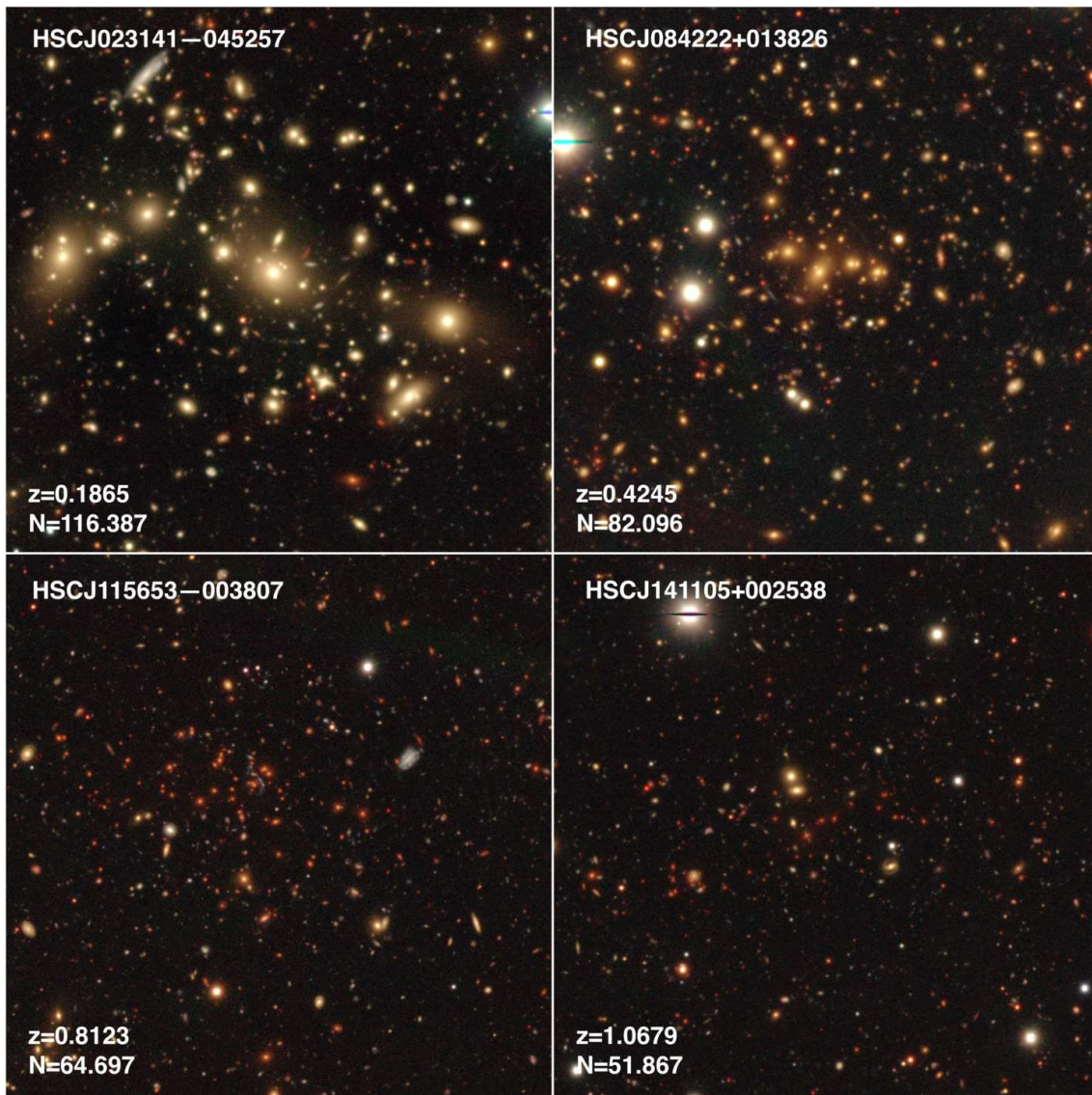


Fig. 5. HSC *grz*-band color composite images of the richest clusters at different redshifts in the HSC Wide S16A cluster catalog. The cluster photometric redshift $z = z_{cl}$ and richness $N = \hat{N}_{mem}$ are indicated in each panel. The size of each panel, which is centered at the BCG identified by the CAMIRA algorithm, is approximately $3'.7 \times 3'.7$. North is up and east is left.

redshift range $0.1 < z_{cl} < 0.6$ and with the corrected richness $\hat{N}_{cor} > 20$.

In Figure 8, we compare the richness from HSC with the incompleteness-corrected richness from SDSS as a function of cluster redshift. While at low redshift these richness agree with each other, at higher redshift ($z \gtrsim 0.3$), where the richness correction is applied to SDSS richness, we find a systematic offset between these two richness, such that richness in HSC is systematically lower than richness in SDSS. This comparison suggests a possible systematic bias in the incompleteness correction in the CAMIRA SDSS cluster catalog, and hence highlights importance of using deep data to detect sufficiently faint cluster members for optical cluster finding. The deep photometric data are also important to study the redshift evolution of the

luminosity function of cluster member galaxies.

5 Comparison with X-ray cluster catalogs

5.1 X-ray catalogs

The footprint of the HSC Wide S16A cluster catalog has a large overlap with two large area X-ray surveys, the XMM Large Scale Structure survey (XMM-LSS; Pierre et al. 2004) and the XXL survey (Pierre et al. 2016). We adopt a sample of 52 X-ray bright clusters selected from the 11 deg^2 XMM-LSS survey region presented in Clerc et al. (2014), and also a sample of 51 X-ray bright clusters from the $\sim 25 \text{ deg}^2$ XXL North survey region presented in Pacaud et al. (2016) and Giles et al. (2016). For both the cluster catalogs, we use X-ray centroids,

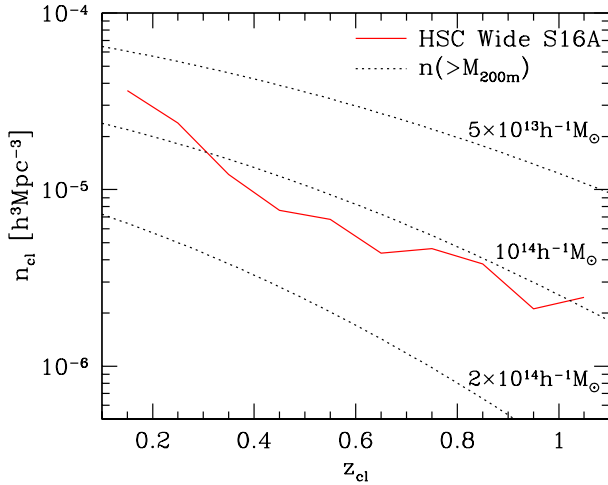


Fig. 6. The comoving number density of HSC Wide S16A clusters as a function of cluster redshift (*solid*). The Poisson error is sufficiently small, $\sim 10\%$ in each bin. Dotted lines show the predicted number densities of halos with masses $M_{200m} > 5 \times 10^{13} h^{-1} M_{\odot}$ (*top*), $10^{14} h^{-1} M_{\odot}$ (*middle*), and $2 \times 10^{14} h^{-1} M_{\odot}$ (*bottom*), which are computed using a halo mass function of Tinker et al. (2008).

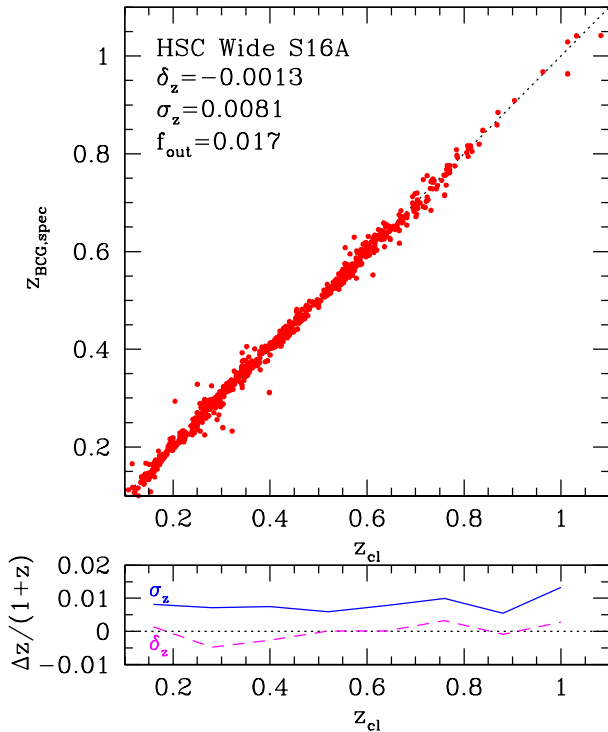


Fig. 7. *Upper:* The comparison between cluster photometric redshifts z_{cl} and spectroscopic redshifts of BCGs $z_{BCG,spec}$. *Lower:* The bias δ_z (*dashed*) and scatter σ_z (*solid*) of the residual $(z_{cl} - z_{BCG,spec})/(1 + z_{BCG,spec})$ as a function of redshift.

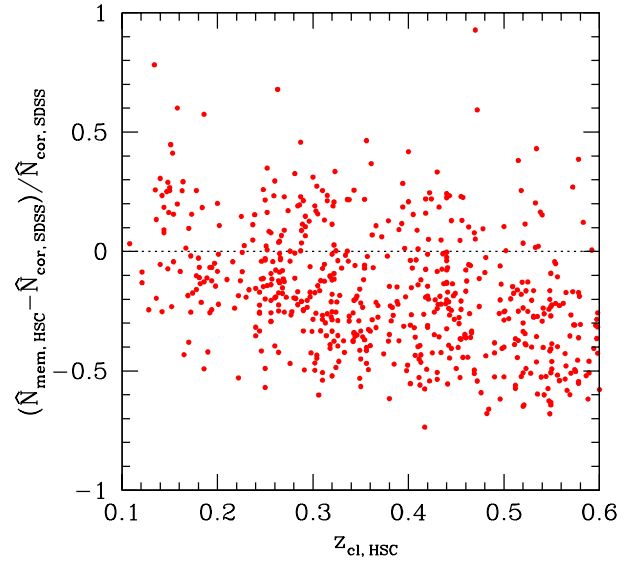


Fig. 8. Comparison of the CAMIRA richness in HSC, $\hat{N}_{mem,HSC}$, with the incompleteness-corrected CAMIRA richness in SDSS, $\hat{N}_{cor,SDSS}$. The fractional difference of these two richness is plotted as a function of cluster redshift from HSC, $z_{cl,HSC}$.

redshifts from the spectroscopy of member galaxies, X-ray temperatures T_X , and rest-frame [0.5–2] keV luminosities within $r_{500,MT}$, $L_{X,500}$, where $r_{500,MT}$ is the radius within which the mean matter density of the cluster becomes 500 times the critical density of the Universe at the cluster redshift with the corresponding mass M_{500} estimated from a mass-temperature relation. In the XXL survey, X-ray temperatures T_X are computed within a fixed aperture of 300 kpc. These two cluster catalogs have some overlap, and in this paper we use values from the XXL catalog when a cluster is included on both the XXL and XMM-LSS catalogs, because the XXL survey is an extension of the XMM-LSS survey. In addition, we remove 4 XXL cluster located at $Dec < -6.6$ as the HSC Wide S16A cluster catalog does not cover that area (see Figure 3).

By combining these two X-ray cluster catalogs, we construct a sample of 77 X-ray bright clusters which are used for characterizing the HSC Wide S16A cluster catalog. The spatial distribution of these X-ray clusters is shown in Figure 3.

5.2 Correlation of richness with X-ray properties

The comparison between the richness and X-ray properties such as the luminosity $L_{X,500}$ and temperature T_X is useful. Because X-ray properties are more tightly correlated with cluster masses (but see also Andreon & Hurn 2010; Andreon 2015), the correlation of richness with X-ray properties is often used as a proxy for the tightness of the correlation between the richness and the cluster mass (e.g., Rykoff et al. 2012; Rozo & Rykoff 2014; Oguri 2014; Wen & Han 2015).

We cross match the HSC Wide S16A cluster catalog with

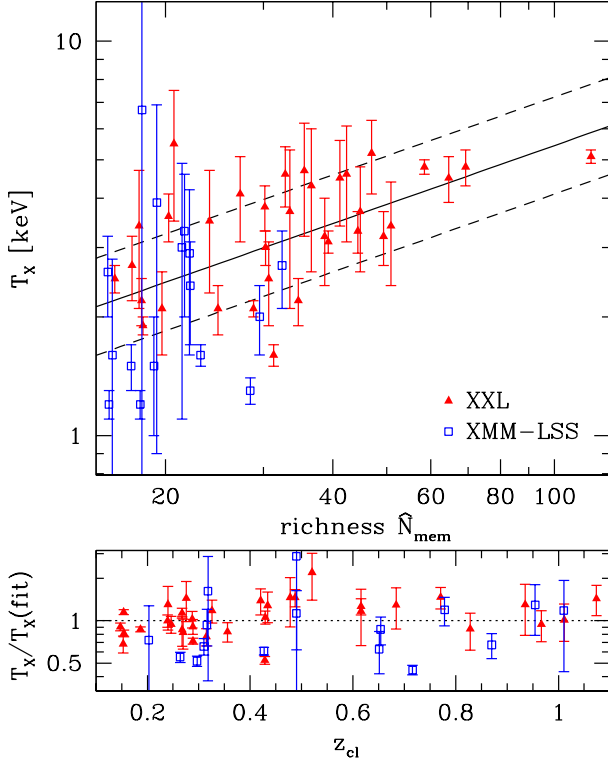


Fig. 9. Comparison between richness \hat{N}_{mem} and X-ray temperature T_X for XXL (filled triangles) and XMM-LSS (open squares) clusters. The solid and dashed lines show the best-fit richness-temperature relation and the range of $\pm 1\sigma$ intrinsic scatter. The lower panel shows the residual of fitting as a function of redshift.

the X-ray cluster catalog constructed in Section 5.1. Again, we use a simple matching criterion that clusters whose physical transverse distance is within $1h^{-1}\text{Mpc}$ and redshift difference is smaller than 0.1 are matched. When there are several matching candidates, we adopt clusters with the smallest transverse separation. Among the 77 X-ray bright clusters from XXL and XMM-LSS, 50 clusters are found to have counterparts in the HSC Wide S16A catalog. Some of the X-ray clusters have no counterpart in the HSC cluster catalog simply because their redshifts fall outside the redshift range of the HSC Wide S16A catalog (i.e., $z < 0.1$ or $z > 1.1$). There are other X-ray clusters that fall within the redshift range of the CAMIRA catalog but have no counterpart, which are used to estimate the completeness of the HSC cluster catalog (see Section 5.3).

Figure 9 compares the richness \hat{N}_{mem} with X-ray temperature T_X for the 50 clusters. There is a clear positive correlation between \hat{N}_{mem} and T_X . To quantify the correlation, we fit the relation assuming the following power law model:

$$\log\left(\frac{T_X}{\text{keV}}\right) = a_T \log\left(\frac{\hat{N}_{\text{mem}}}{30}\right) + b_T. \quad (7)$$

This model is same as that used in Oguri (2014) except that the pivot richness is changed to 30. We find the best-fit parameters of $a_T = 0.50 \pm 0.12$ and $b_T = 0.48 \pm 0.02$. The slope

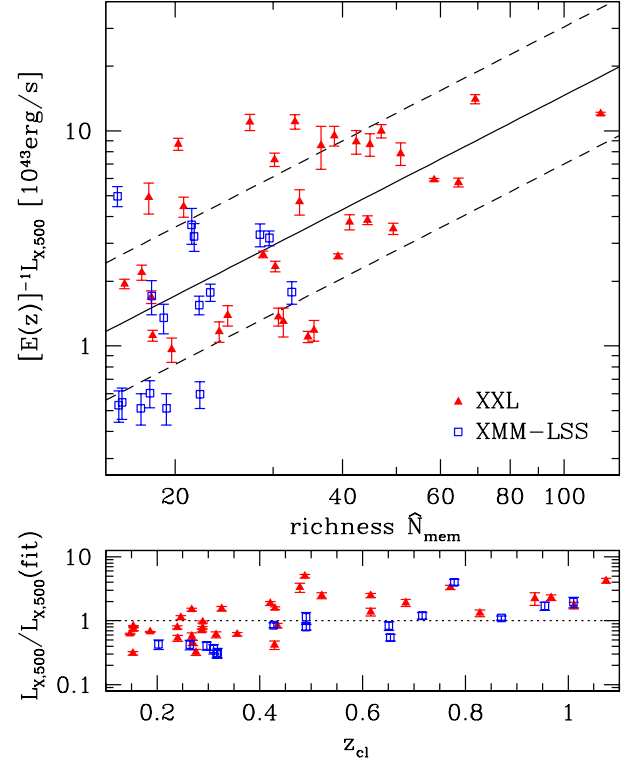


Fig. 10. Same as Figure 9, except that the comparison between richness \hat{N}_{mem} and evolution-corrected X-ray luminosity $[E(z)]^{-1} L_{X,500}$ is shown.

$a_T = 0.50$ is shallower than $2/3$ predicted from $M \propto \hat{N}_{\text{mem}}$ and the self-similar model $T_X \propto M^{2/3}$. The relation also implies that the mass limit of the HSC cluster catalog of $M_{500c} \gtrsim 2 \times 10^{14} h^{-1} M_\odot$ (Lieu et al. 2016) which is broadly consistent with the mass limit from the number density (Section 3.2). We also find 1σ intrinsic scatter of 0.12 in $\log T_X$, which is comparable to the scatter for the SDSS CAMIRA and redMaPPer cluster catalogs (Rozo & Rykoff 2014; Oguri 2014). Figure 9 also suggests that there is no strong redshift evolution of this relation.

We then compare \hat{N}_{mem} with X-ray luminosity $L_{X,500}$ for the same clusters in Figure 10. It has been shown that the L_X - T_X relation evolves with redshift such that $E(z)^{-\gamma_{LT}} L_X \propto T_X^B$, where $E(z) = \sqrt{\Omega_M(1+z)^3 + \Omega_\Lambda}$, $B \sim 3$, and the self-similar model predicts $\gamma_{LT} = 1$ (e.g., Giles et al. 2016). We include the effect of redshift evolution by studying the correlation between \hat{N}_{mem} and evolution-corrected X-ray luminosity $[E(z)]^{-1} L_{X,500}$ assuming the self-similar evolution $\gamma_{LT} = 1$. As before, Figure 10 indicates a good correlation between the richness and X-ray luminosity. We quantify this by fitting it to a power-law model:

$$\log\left(\frac{[E(z)]^{-1} L_{X,500}}{10^{43} \text{erg/s}}\right) = a_L \log\left(\frac{\hat{N}_{\text{mem}}}{30}\right) + b_L, \quad (8)$$

and find $a_L = 1.33 \pm 0.24$, $b_L = 0.47 \pm 0.05$, and the intrinsic scatter $\sigma = 0.32$.

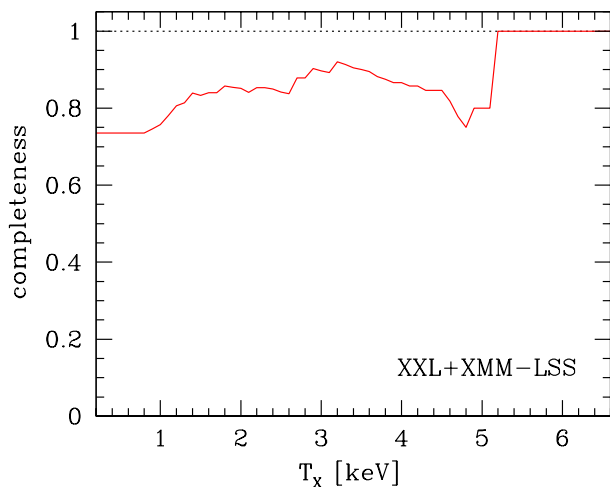


Fig. 11. Completeness of HSC Wide S16A clusters which is estimated using X-ray clusters. The completeness is defined by the fraction of X-ray clusters that match the HSC cluster catalog to all X-ray clusters. The completeness is estimated as a function of X-ray temperature threshold (i.e., for each T_X all X-ray clusters with $> T_X$ are used to derive the completeness).

The residual of fitting as a function of redshift shown in Figure 10 indicates a clear trend with redshift. This may suggest a redshift evolution stronger than the self-similar prediction, i.e., $\gamma_{LT} > 1$ (see also Giles et al. 2016), although it must be partly due to the Malmquist bias. This is because the X-ray cluster sample is a flux-limited sample and X-ray luminosities are more directly related to X-ray fluxes. The idea is supported by the fact that XMM-LSS clusters, which have the lower X-ray flux limit, tend to have lower luminosities than those of XXL clusters at all redshift range. Hence in order to derive the intrinsic scaling relation we need to take account of flux limits of these X-ray surveys, which we leave for future work.

5.3 Completeness estimation

In addition to using mocks (see Section 6), we estimate the completeness of the HSC Wide S16A catalog using the X-ray cluster catalog. Here we adopt a simple approach to estimate the completeness by the fraction of X-ray clusters with optical counterparts to all X-ray clusters. Given an ambiguity of matching between HSC and X-ray clusters, the completeness presented here should be interpreted with caution. We derive the completeness as a function of X-ray temperature threshold; for a given T_X , we use all X-ray cluster above T_X to derive the completeness. We also restrict the redshift range of the X-ray clusters to $0.1 < z < 1.1$ for the completeness estimation.

Figure 11 plots the estimated completeness as a function of X-ray temperature threshold. We find that the completeness is generally high, $\sim 0.8-0.9$. There are a couple of X-ray clusters with relatively high X-ray temperatures, $T_X \sim 5$ keV, which do not have counterparts in the HSC cluster catalog. We find that

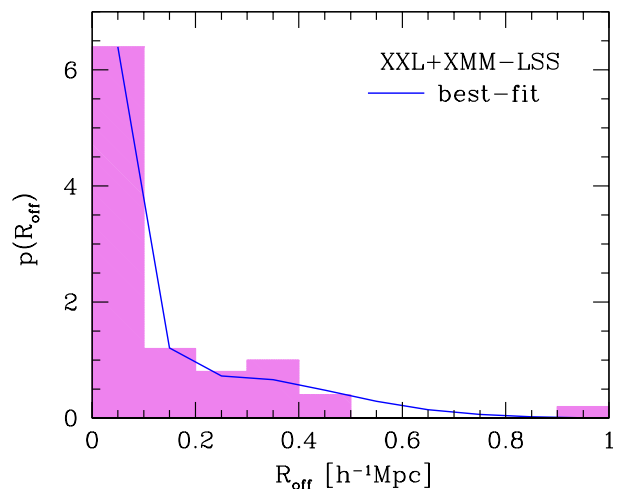


Fig. 12. Distribution of positional offset between HSC Wide S16A clusters and X-ray clusters, which is derived using 50 X-ray clusters from XXL and XMM-LSS surveys that matches the HSC cluster catalog. The offsets R_{off} are defined by physical transverse distances between HSC and X-ray cluster centers. The solid line shows the best-fit model assuming the functional form of equation (9).

these X-ray clusters have companion X-ray clusters separated by $\sim 8'$ at similar redshifts. For example, one of them corresponds to a member of a supercluster of galaxies at $z = 0.43$ (Pompei et al. 2016). Since the CAMIRA algorithm adopts a compensated spatial filter for creating a richness map (Oguri 2014), detections of companion clusters near massive clusters tend to be suppressed, as also noted in Miyazaki et al. (2015). The current analysis of completeness is limited by a small number of X-ray sample, and an extended analysis using a larger sample of X-ray clusters is useful for quantifying the impact of paired clusters on the completeness.

5.4 Positional offset distribution

It has been known that optical cluster finders often misidentify centers of clusters. This miscentering effect is important for applications of optically-selected clusters such as weak lensing analysis. Miscentering of optically-selected clusters have indeed been studied with various approaches, including offsets between optical and X-ray cluster centers (e.g., Lin et al. 2004; Mahdavi et al. 2013; Rozo & Rykoff 2014; Oguri 2014; Rykoff et al. 2016), offsets between optical and SZ cluster centers (e.g., Song et al. 2012; Sehgal et al. 2013; Sifón et al. 2013; Saro et al. 2015), and weak lensing (e.g., Oguri et al. 2010; George et al. 2012; Oguri 2014; Ford et al. 2014; Viola et al. 2015; van Uitert et al. 2016; Miyatake et al. 2016). In this paper we use offsets between HSC Wide S16A clusters, whose centers are defined by the locations of BCGs identified by the CAMIRA algorithm (see Oguri 2014), and the X-ray clusters from XXL and XMM-LSS to study the miscentering effect.

Figure 12 shows the offset (physical transverse distance

R_{off}) distribution derived from the 50 X-ray clusters that are matched with the HSC Wide S16A cluster catalog. In the HSC Wide S16A cluster catalog, cluster centers are defined by centroids of BCGs identified by the CAMIRA algorithm. The distribution is clearly peaked at $R_{\text{off}} \sim 0$, indicating that HSC Wide S16A clusters are well centered on average. On the other hand, there is also a tail toward large R_{off} , as has been found in other optically-selected cluster catalogs. We fit the measured distribution to the following two-component Gaussian model (e.g., Oguri & Takada 2011)

$$p(R_{\text{off}}) = f_{\text{cen}} \frac{R_{\text{off}}}{\sigma_1^2} \exp\left(-\frac{R_{\text{off}}^2}{2\sigma_1^2}\right) + (1 - f_{\text{cen}}) \frac{R_{\text{off}}}{\sigma_2^2} \exp\left(-\frac{R_{\text{off}}^2}{2\sigma_2^2}\right). \quad (9)$$

We simultaneously fit the fraction of well-centered clusters, f_{cen} , the standard deviation for the well-centered population, σ_1 , and the standard deviation for the miscentered population, σ_2 . The best-fit parameters are $f_{\text{cen}} = 0.68 \pm 0.09$, $\sigma_1 = 0.046 \pm 0.009 h^{-1} \text{Mpc}$, and $\sigma_2 = 0.26 \pm 0.04 h^{-1} \text{Mpc}$. We confirmed that fitting results with smaller bin sizes are consistent with the result above within the error bars. The best-fit model shown in Figure 12 indicates that the two-component model fits the observation reasonably well.

We check the possible richness dependence of the offset distribution by dividing the cluster catalog into two richness bins, $\hat{N}_{\text{mem}} < 30$ and $\hat{N}_{\text{mem}} > 30$, and repeating the analysis above. Given the smaller number of X-ray clusters in each richness bin, we fix σ_1 and σ_2 to the best-fit values obtained from the analysis of the full sample, and fit only f_{cen} . We find that $f_{\text{cen}} = 0.66 \pm 0.10$ for $\hat{N}_{\text{mem}} < 30$, and $f_{\text{cen}} = 0.71 \pm 0.12$ for $\hat{N}_{\text{mem}} > 30$, which indicates that there is no strong dependence of the offset distribution on richness.

6 Analysis of mock galaxy samples

6.1 Construction of mock galaxy samples

We create mock galaxy samples specifically designed for testing cluster finding algorithms. Since accurate galaxy colors are crucial for this purpose, we use colors of true observed galaxies in the HSC Survey. We use the HSC galaxy catalog in the COSMOS (Scoville et al. 2007) field for the field galaxy population, and use CAMIRA clusters in HSC Wide S16A to select cluster member galaxies. N -body simulations are used to produce realistic distributions of halo masses and redshifts. Thus our mock galaxy catalogs use realistic cluster distributions, and also contain gaps and holes in the spatial distribution of galaxies due to bright stars and bad columns, which allow realistic characterization of completeness and purity. We provide a detailed description of our mock galaxy samples in Appendix 3.

We note that we need to make assumptions on the input

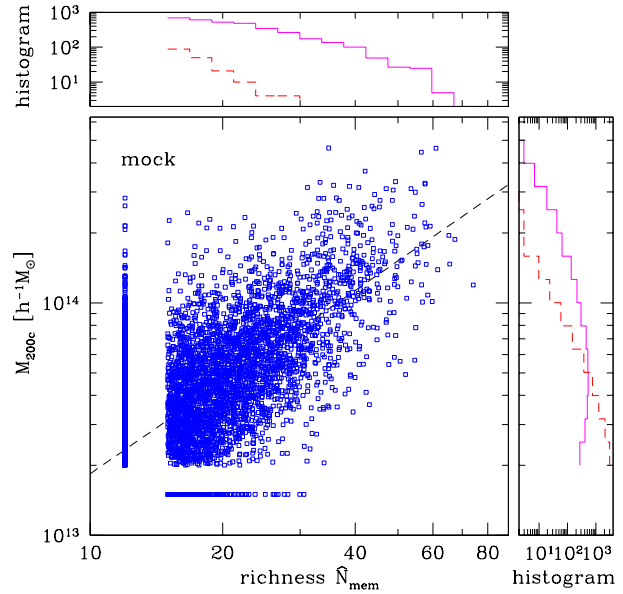


Fig. 13. Comparison of cluster richness \hat{N}_{mem} and halo mass M_{200c} from the analysis of mock galaxy catalogs (see Section 6.1 for the description). For illustrative purpose, we assign $\hat{N}_{\text{mem}} = 12$ for halos without any counterpart in the cluster catalog, and $M_{200c} = 1.5 \times 10^{13} h^{-1} M_{\odot}$ for clusters without any counterpart in the halo catalog. The dashed line shows a power-law fit to $(\log M | N)$ using the matching result with $\hat{N}_{\text{mem}} > 20$ (see equation 11). In the upper and right panels, we also show the histograms of matched (solid) and unmatched (dashed) clusters/halos.

richness-mass relation, red galaxy fraction, and their redshift evolution in order to create these mock galaxy samples, which may not necessarily be correct. While quantitative results such as the scatter in the observed richness-mass relation and the completeness as a function of halo masses depend on these assumptions, we expect that the qualitative behavior of the completeness and purity estimated from these mocks is not very sensitive to these assumptions.

6.2 Analysis results

We run the CAMIRA algorithm on the mock galaxy samples using the same setup as the one used to create the HSC Wide S16A catalog. We then cross match CAMIRA cluster catalogs on the mocks with input halo catalogs. We use the matching criterion of the physical transverse distance being smaller than $1 h^{-1} \text{Mpc}$ and the difference between the halo redshift and the cluster photometric redshift being smaller than 0.1. Given the limited range of the redshift and halo mass of our mock galaxy samples (see Appendix 3), we also restrict the redshift range of halos to $0.3 < z_{\text{halo}} < 1.0$ and the mass range to $M_{200c} > 2 \times 10^{13} h^{-1} M_{\odot}$ in cross-matching. We record all clusters and halos that fall within the same redshift range but fail to match, which are used to estimate completeness and purity below. We analyze 90 realizations of the COSMOS-size mock galaxy samples, leading to the total area of $\sim 144 \text{ deg}^2$.

Figure 13 shows the result of matching. As expected we can clearly see a positive correlation between halo masses and richness. We find that most of the CAMIRA clusters in the mocks have counterparts in the halo catalog except for the very low richness end, which indicates that the purity of the CAMIRA cluster catalog, which is defined by the fraction of CAMIRA clusters that corresponds to real massive halos, is high, > 0.95 down to the richness limit of $\hat{N}_{\text{mem}} = 15$. On the other hand, Figure 13 indicates that there are halos up to $\sim 10^{14} h^{-1} M_{\odot}$ that are not detected by the CAMIRA algorithm, which implies that the completeness, which is defined by the fraction of halos that are correctly identified by the CAMIRA algorithm, requires careful studies.

Our CAMIRA cluster sample is constructed in the limited richness range of $\hat{N}_{\text{mem}} > 15$, which may impact on the estimate of the completeness as a function of halo mass. We derive a simple correction of the effect of the lower limit of the richness by assuming a log-normal form for the mass-richness relation

$$p(\log M|N) = \frac{1}{\sqrt{2\pi}\sigma_{\log M}} \exp\left[-\frac{(\log M - \langle \log M|N \rangle)^2}{2\sigma_{\log M}^2}\right], \quad (10)$$

here we adopt simplified notations, $N = \hat{N}_{\text{mem}}$ and $M = M_{200c}$ in units of $h^{-1} M_{\odot}$. For the median richness-mass relation $\langle \log M|N \rangle$, we assume the following power-law form

$$\langle \log M|N \rangle = a_M \log\left(\frac{N}{30}\right) + b_M. \quad (11)$$

To derive the parameters, we use the matching result only with $N > 20$ in order to reduce the effect of lower mass limit and perform fitting. The resulting parameters are $a_M = 1.31$, $b_M = 13.89$, and $\sigma_{\log M} = 0.19$. We also confirm that the log-normal model reproduces the observed distribution of halo masses around the median richness-mass relation reasonably well.

The Bayes theorem suggests that $p(\log M|N)$ can be converted to $p(\log N|M)$ via

$$p(\log N|M) = \frac{p(\log M|N)p(\log N)}{\int d(\log N)p(\log M|N)p(\log N)}. \quad (12)$$

Using the locally power-law model (Rozo et al. 2014), it is shown that this distribution has a log-normal distribution with the mean and variance of

$$\langle \log N|M \rangle = \frac{\log M - b_M}{a_M} - \frac{\beta \ln 10}{a_M^2} \sigma_{\log M}^2, \quad (13)$$

$$\sigma_{\log N} = \frac{1}{a_M} \sigma_{\log M}, \quad (14)$$

where β is the slope of the richness function, $p(\log N) \propto dn/d\log N \propto N^{-\beta}$. We assume $\beta = 1$ for simplicity, which is broadly consistent with the observed richness distribution near the richness threshold. We can then compute the selection function (or completeness) for a sample with $N > N_{\text{lim}}$ predicted by the log-normal model as

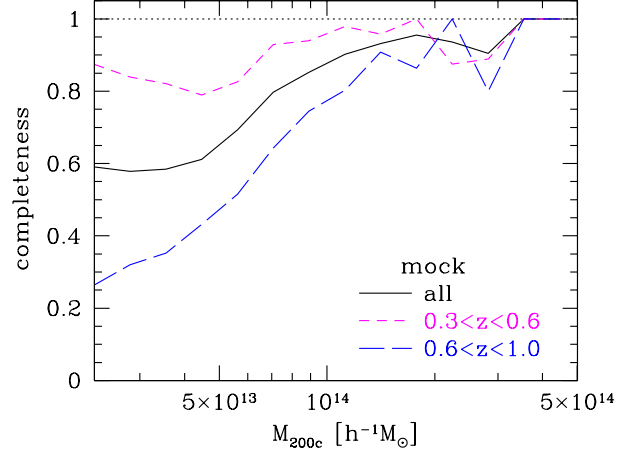


Fig. 14. Completeness estimated from the analysis of mock galaxy catalogs as a function of halo mass M_{200c} . The completeness is defined by equation (16). The solid line shows the completeness using all halos. Short-dashed and long-dashed lines indicate the completeness for subsamples of halos at $0.3 < z < 0.6$ and $0.6 < z < 1.0$, respectively.

$$\begin{aligned} S(M|N > N_{\text{lim}}) &= \frac{p(\log M|N > N_{\text{lim}})}{p(\log M)} \\ &= \int_{N_{\text{lim}}}^{\infty} p(\log N|M) d(\log N) \\ &= \frac{1}{2} \text{erfc} \left[\frac{\log N_{\text{lim}} - \langle \log N|M \rangle}{\sqrt{2}\sigma_{\log N}} \right]. \end{aligned} \quad (15)$$

The completeness we are interested in here is the completeness that cannot be explained by a simple extrapolation of the mass-richness relation. To derive this, we first prepare a sample of CAMIRA clusters in the mocks with $N > N_{\text{lim}}$ that successfully match to the halo catalog. We denote the number distribution of these clusters as $n_{\text{obs}}(M|N > N_{\text{lim}})$. From the original halo catalog, we can also derive the number distribution of all halos, $n(M)$. We estimate the completeness, for which the effect of the lower limit of richness is corrected, as

$$\text{completeness} = \frac{n_{\text{obs}}(M|N > N_{\text{lim}})}{n(M)S(M|N > N_{\text{lim}})}. \quad (16)$$

Put another way, this provides the incompleteness of identifying halos that cannot be explained by a simple extrapolation of the mass-richness relation.

Figure 14 shows the completeness defined by equation (16). Here we adopt $N_{\text{lim}} = 15$, although the result is insensitive to the specific choice of N_{lim} as expected. We note that, for $N_{\text{lim}} = 15$, the correction factor $S(M)$ is very close to unity down to $M_{200c} \sim 10^{14} h^{-1} M_{\odot}$ and decreases to ~ 0.5 at $M_{200c} \sim 3 \times 10^{13} h^{-1} M_{\odot}$, and hence the correction of the completeness due to $S(M)$ is relatively minor. We find that the completeness after the N_{lim} correction is reasonably high (> 0.9) at high mass end, $M_{200c} \gtrsim 10^{14} h^{-1} M_{\odot}$, and decreases below $10^{14} h^{-1} M_{\odot}$. This result is also broadly consistent with the completeness estimated from X-ray clusters shown in Figure 11. A possible explanation of decreasing completeness at low mass

end is that the scatter in the richness-mass relation increases rapidly toward lower richness, due to the larger Poisson noise of the number of cluster member galaxies and more significant contribution of background fluctuations to the richness that enhances the scatter. In either case, the high completeness at high cluster masses is encouraging from the viewpoint of using massive optically-selected clusters as a cosmological probe.

It is possible that the completeness changes with redshift. To check the possible redshift dependence, we divide the mock halo sample into two redshift bins with $0.3 < z < 0.6$ and $0.6 < z < 1.0$, and derive completeness for both the subsamples. The result shown in Figure 14 indicates that the completeness indeed depends on the redshift. For the low-redshift halos, the completeness remains high down to $\sim 8 \times 10^{13} h^{-1} M_{\odot}$, whereas for high-redshift halos the completeness starts to drop at higher masses. Decreasing completeness with increasing redshift for a fixed halo mass may be partly due to decreasing red galaxy fraction which is taken into account in the mock galaxy catalog construction (see Appendix 3). In both redshift bins the completeness is close to unity above $\sim 1.5 \times 10^{14} h^{-1} M_{\odot}$. This redshift evolution of the completeness should also be taken into account for careful statistical studies of CAMIRA clusters.

Again, we emphasize that our quantitative results from the mock catalog depend on input models, such as cosmological parameters and mass-richness relations for populating galaxies in halos, which can differ from true values. For example, the redshift evolution of the completeness discussed above depends crucially on the redshift evolution of the input mass-richness relation and the input redshift evolution of the red fraction in clusters (see Appendix 3). In particular, we note that our current mock catalog appears to overestimate richness in the sense that the number density of CAMIRA-detected clusters in the mock as a function of richness is a factor of ~ 4 higher than in observations, which suggests room for improvements of the mock. Nevertheless, the mock result should still be useful for understanding qualitative behavior of the completeness and purity of the CAMIRA algorithm, and both the mock catalog analysis presented here and the comparison with other (such as X-ray) cluster catalogs as presented in Section 5 are important for characterizing the CAMIRA cluster catalog.

7 Summary

We have presented a new optically-selected cluster catalog from the HSC Survey. From the HSC Wide S16A dataset covering $\sim 232 \text{ deg}^2$, we have constructed a sample of 1921 clusters at redshift $0.1 < z_{\text{cl}} < 1.1$ and with richness $\tilde{N}_{\text{mem}} > 15$. Based on the number density, we infer that the rough mass limit of the cluster sample is $M_{200\text{m}} \gtrsim 10^{14} h^{-1} M_{\odot}$. We have found that cluster redshifts are accurate with the bias $\delta_z < 0.005$ and the scatter $\sigma_z < 0.01$ for most of the redshift range. The photomet-

ric redshift accuracy is comparable to that of optically-selected clusters in SDSS, but HSC clusters extend to much higher redshifts. We have also compared the HSC Wide S16A cluster catalog with X-ray clusters from XXL and XMM-LSS surveys, finding tight correlations between richness and X-ray properties. In addition, we have derived the distribution of positional offsets of cluster centers using the X-ray clusters and found that the fraction of well-centered clusters is ~ 0.7 , with no significant dependence on richness. We have analyzed mock galaxy catalogs to study the completeness and purity. We have found a high purity, and also the high completeness for halos with masses above $\sim 10^{14} h^{-1} M_{\odot}$. The completeness depends on redshift such that completeness for lower mass halos is higher at lower redshift.

This work presents the first cluster catalog from the HSC Survey, and demonstrates the power of the HSC Survey for studies of high-redshift clusters. The exquisite depth of the HSC Survey allows us to detect almost all cluster member galaxies above $M_* \sim 10^{10.2} M_{\odot}$ even at $z \sim 1.1$, and hence allows a reliable cluster search at such high redshifts. For instance, by extrapolating the result in this paper, we expect to construct a large catalog of ~ 1000 clusters with richness $\tilde{N}_{\text{mem}} > 20$ at $z \sim 1$ from the final HSC Wide Survey dataset covering $\sim 1400 \text{ deg}^2$. We plan to calibrate cluster masses using stacked weak lensing technique, as well as careful comparisons with X-ray and SZ cluster catalogs, including an extended XXL X-ray cluster catalog and SZ clusters from ACTPol (Niemack et al. 2010).

Acknowledgments

We thank Cristóbal Sifón for useful comments, and an anonymous referee for useful suggestions. This work is supported in part by World Premier International Research Center Initiative (WPI Initiative), MEXT, Japan, and JSPS KAKENHI Grant Number 26800093. This work is in part supported by MEXT Grant-in-Aid for Scientific Research on Innovative Areas (No. 15H05887, 15H05892, 15H05893). YTL acknowledges support from the Ministry of Science and Technology grants MOST 104-2112-M-001-047 and MOST 105-2112-M-001-028-MY3. HM is supported by the Jet Propulsion Laboratory, California Institute of Technology, under a contract with the National Aeronautics and Space Administration.

The Hyper Suprime-Cam (HSC) collaboration includes the astronomical communities of Japan and Taiwan, and Princeton University. The HSC instrumentation and software were developed by the National Astronomical Observatory of Japan (NAOJ), the Kavli Institute for the Physics and Mathematics of the Universe (Kavli IPMU), the University of Tokyo, the High Energy Accelerator Research Organization (KEK), the Academia Sinica Institute for Astronomy and Astrophysics in Taiwan (ASIAA), and Princeton University. Funding was contributed by the FIRST program from Japanese Cabinet Office, the Ministry of Education, Culture, Sports, Science and Technology (MEXT), the Japan Society for the Promotion of Science (JSPS), Japan Science and Technology Agency (JST), the Toray Science Foundation, NAOJ, Kavli IPMU, KEK, ASIAA, and Princeton University.

The Pan-STARRS1 Surveys (PS1) have been made possible through

contributions of the Institute for Astronomy, the University of Hawaii, the Pan-STARRS Project Office, the Max-Planck Society and its participating institutes, the Max Planck Institute for Astronomy, Heidelberg and the Max Planck Institute for Extraterrestrial Physics, Garching, The Johns Hopkins University, Durham University, the University of Edinburgh, Queen's University Belfast, the Harvard-Smithsonian Center for Astrophysics, the Las Cumbres Observatory Global Telescope Network Incorporated, the National Central University of Taiwan, the Space Telescope Science Institute, the National Aeronautics and Space Administration under Grant No. NNX08AR22G issued through the Planetary Science Division of the NASA Science Mission Directorate, the National Science Foundation under Grant No. AST-1238877, the University of Maryland, and Eotvos Lorand University (ELTE).

This paper makes use of software developed for the Large Synoptic Survey Telescope. We thank the LSST Project for making their code available as free software at <http://dm.lsst.org>.

Based [in part] on data collected at the Subaru Telescope and retrieved from the HSC data archive system, which is operated by the Subaru Telescope and Astronomy Data Center at National Astronomical Observatory of Japan.

Appendix 1. Cluster catalogs

We construct three cluster catalogs from the HSC S16A data. The first catalog is from the Wide region without applying for a bright star mask. This catalog is used in the analysis throughout the paper. The second catalog is also from the Wide region, but with the bright star mask. The bright star mask removes object near bright stars, and the current mask is designed conservatively such that it removes nearly $\sim 10\%$ of objects. The current cluster catalog with the star mask suffers from the effect of masking bright galaxies, which is discussed in Appendix 2. The third catalog is from the Deep region covering $\sim 25 \text{ deg}^2$. Even though the Deep data are deeper than the Wide data, we use the same selection criteria for constructing an input galaxy catalog, including the conservative z -band magnitude limit of $z < 24$. These catalogs are shown in Supplementary Tables 1, 2, and 3.

Appendix 2. Effect of the bright star mask on cluster finding

In addition to overly conservative sizes of mask regions, a known issue of the current version of the bright star mask is that it also masks bright nearby galaxies (Aihara et al. 2017). This is because a bright object catalog from the Naval Observatory Merged Astrometric Dataset (NOMAD; Zacharias et al. 2005), which we use to select mask regions, often misinterprets nearby bright galaxies as stars. We check the impact of masking bright galaxies on cluster finding by comparing cluster catalogs with and without star masks.

We match HSC Wide S16A cluster catalogs with and without the bright star mask in the same manner as in Section 4. The comparison of cluster photometric redshifts shown in Figure 15

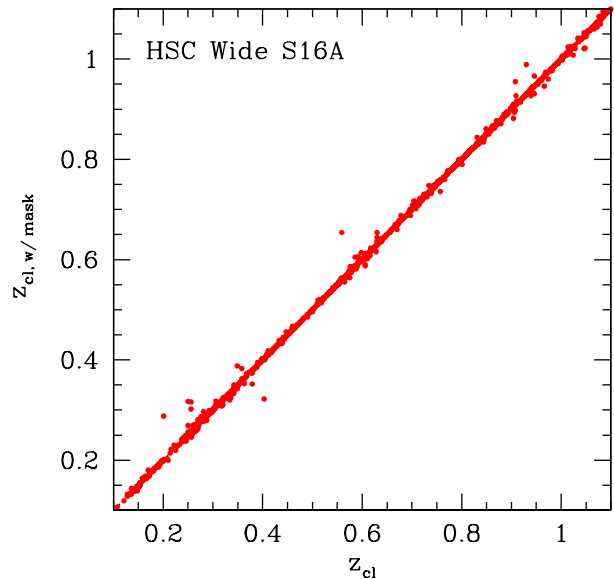


Fig. 15. The comparison of cluster photometric redshifts z_{cl} between HSC Wide S16A cluster catalogs with and without the bright star mask.

indicates that photometric redshifts agree well between these two cluster catalogs. In contrast, the comparison of richness in Figure 16 shows a clear bias at low redshifts, $z \lesssim 0.4$, such that richness in the cluster catalog with the bright star mask is systematically lower than in the cluster catalog without the bright star mask. We find that this is due to masking of bright galaxies as mentioned above, which masks red member galaxies near BCGs, as well as BCGs themselves, leading to smaller richness estimates for those clusters. Therefore, for any cluster studies that involve low-redshift clusters, we recommend not to use the cluster catalog with the bright star mask. For studies of high-redshift ($z \gtrsim 0.4$) clusters, however, the effect of masking bright galaxies is negligible and we expect we can safely use the cluster catalog with the bright star mask.

As discussed in Aihara et al. (2017), we are working on revising the bright star mask, and we expect that this issue will be resolved in future versions of HSC CAMIRA cluster catalogs.

Appendix 3. Description of the mock galaxy catalog

The set of mock galaxy catalogs we use for testing the cluster finding algorithm is produced by combining a “field” galaxy population with a “cluster” galaxy population. In a nutshell, the “field” population is generated from well-studied extragalactic fields with rich multiwavelength data (particularly in X-rays), so that galaxies associated with massive galactic systems such as clusters and groups can be removed (leaving only the field galaxies). On the other hand, the “cluster” population is obtained by populating dark matter halos with galaxies from real, observed clusters. Below we briefly describe how each of these

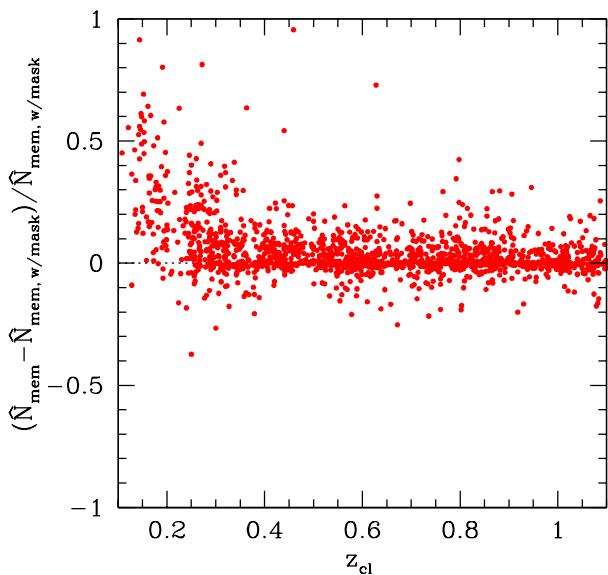


Fig. 16. The comparison of richness \hat{N}_{mem} between HSC Wide S16A cluster catalogs with and without the bright star mask.

is produced.

For the field galaxy catalog, we use the HSC Subaru Strategic Program observation of the COSMOS (Scoville et al. 2007) field as the parent sample. More specifically, we adopt the Wide-layer depth *grizy*-band photometry of the Ultradeep-layer observation. We further remove galaxies that are likely associated with known structures in the COSMOS field, such as galaxy groups and clusters, by excluding ~ 4000 galaxies that have membership probability $P_{\text{mem}} > 0.5$ according to the galaxy group catalog of George et al. (2011).

For generating the cluster galaxy catalog, our first step is to extract halo catalogs from a lightcone constructed from a large N -body simulation (see Sehgal et al. 2010 for more details of the simulation and the lightcone creation). The halos are extracted from the N -body simulation which has a box size of $1000 h^{-1} \text{Mpc}$, using a friends-of-friends algorithm with a linking length of 0.2 mean particle separation. In summary, the lightcone is complete for halos with $M_{200c} \geq 10^{13} M_{\odot}$ and $z \leq 3$. We consider a patch in the lightcone that is of the same geometry and area as the COSMOS field, and only include halos at $z < 1.2$. We then populate these halos with galaxies that are probable members of real clusters and groups observed by the HSC, following a galaxy number–halo mass relation

$$N(M, z) = A \left(\frac{M_{200c}}{10^{14} M_{\odot}} \right)^b (1+z)^c \quad (17)$$

with $A = 47$, $b = 0.85$, $c = -0.1$, which is consistent with observations of Lin et al. (2004, 2006) for galaxies more luminous than $M^*(z) + 4$, where M^* is the evolving characteristic magnitude of the galaxy luminosity function in z -band. We note that the definition of this input N differs from the richness in CAMIRA. The input richness is defined for all cluster mem-

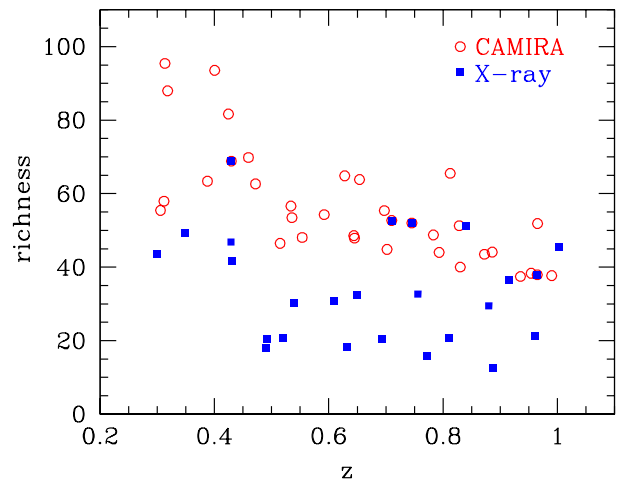


Fig. 17. Comparison of the clusters used to “populate” the halos between our default set (open circles; 35 clusters) and the test set (filled square; 25 clusters). The default set uses richest CAMIRA clusters, while the test set employs those CAMIRA clusters that are also detected in the X-rays, which are mostly from the XXL and XMM Cluster Survey (XCS; Mehrrens et al. 2012).

ber galaxies rather than red member galaxies used in CAMIRA, and also has a different luminosity threshold. Given a halo mass M_{200c} , we draw a Poisson random number with the mean given by the above expression as the total number N of galaxies to be assigned to the halo. The partition of red and blue galaxies is specified by a red fraction function, following the fitting formula of Hansen et al. (2009),

$$f_{\text{red}}(N, z) = g(z) \text{erf}[\log N - \log h(z)] + 0.69, \quad (18)$$

where $g(z) = 0.206 - 0.371z$, $h(z) = -3.6 + 25.8z$. We note that the fitting formula of Hansen et al. (2009) was defined in the redshift range $0.1 \leq z \leq 0.3$, and we extrapolate this result to $z = 1.2$, mainly because of the lack of detailed quantitative studies of red fractions at high redshifts. Since the redshift evolution of the completeness and purity estimated from mock catalogs crucially depend on the input redshift evolution of the red fraction, our mock result should be taken with caution. The numbers of red and blue galaxies of the halo in question are $N_{\text{red}} = f_{\text{red}}N$ and $N_{\text{blue}} = (1 - f_{\text{red}})N$, respectively. The rationale behind the adaptation of a red fraction function is that, due to projection effects, the blue-cloud galaxies usually outnumber that of red-sequence ones, and thus if one simply draws in random N galaxies the color distribution will be strongly biased and uncharacteristic of cluster galaxies.

As for the actual cluster member galaxy data used in this procedure, we have selected the top 5 richest clusters detected by CAMIRA in each of the redshift bins from $z = 0.3$ to $z = 1.0$ with bin width of 0.1. For each of these real clusters, we initially consider all galaxies lying within a projected distance of \tilde{R}_{200c} . Here \tilde{R}_{200c} is a rough estimate of the true value for these massive clusters, obtained by taking average of 5 richest mock clus-

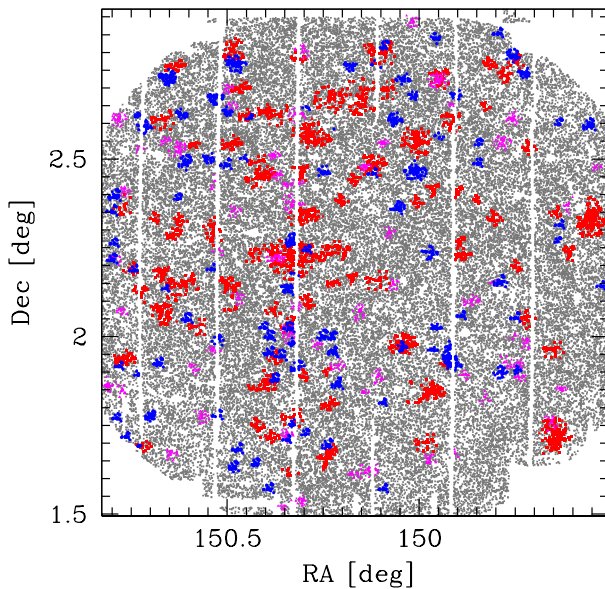


Fig. 18. An example of our mock galaxy catalogs for testing cluster finding algorithms. Small gray dots show the distribution of “field” galaxies, taken from real HSC observations. Red squares, magenta triangles, and blue circles show the distribution of “cluster” galaxies at redshift $0.3 < z < 0.6$, $0.6 < z < 0.9$, and $0.9 < z < 1.2$, respectively.

ters from the public MICE mock catalog (Carretero et al. 2015) selected in the same redshift range, over an area of 200 deg^2 . The subsequent treatment is different for red and blue galaxies. For the galaxies on the red sequence, we simply select the needed N_{red} galaxies, giving preference to the brighter galaxies, using simple red galaxy selections in the color-magnitude diagram. A caveat is that this procedure of populating red galaxies from brighter to fainter galaxies using the richest clusters may introduce bias in mock galaxy population, such as the overestimate of the bright end of the low-mass clusters luminosity functions, which is ignored here. For the blue galaxies, we use photometric redshifts (using EAZY; Brammer et al. 2008) derived from the HSC Survey data to facilitate the selection, taking into account the accuracy of the photometric redshift as a function of magnitude, and draw in random N_{blue} galaxies from the blue cloud by giving higher priority to brighter galaxies. For a given halo in the lightcone, we select the real cluster that is closest in terms of both redshift and richness. To account for the fact that real clusters do not lie at the same redshifts of the halos, we use a passively evolving stellar population model based on the Bruzual & Charlot (2003) model to shift the real galaxies either forward or backward in time with a typical magnitude shift of 0.03. Finally, while we keep the relative orientation of galaxies with respect to the cluster center (defined to be the location of the brightest cluster galaxy), we rescale the radial distance by

² Once the richness-mass relation is calibrated via weak lensing from the HSC survey itself, we will use it for the initial estimate of R_{200} , thus bypassing this step.

the halo mass, assuming an NFW profile (Navarro et al. 1997) with the concentration parameter of $c = 5$. The value of the concentration parameter we adopted is a typical value for the dark matter distribution of halos with masses and redshifts of our interest (e.g., Gao et al. 2008).

In principle, we could include member galaxies in clusters selected by other means, such as X-ray or SZ effect. For the current version of the mock, we have opted to use CAMIRA-selected clusters as these are detected over much larger area than existing X-ray surveys, and thus represent currently the best available massive cluster sample. As an exploratory example, we also attempt another set of mocks (hereafter referred to as the “test set”), which differs from our default set in the source of input clusters. Instead of using the richest CAMIRA clusters, we resort to known X-ray clusters covered by the current HSC footprint that are also matched to the CAMIRA cluster catalog. As mentioned above, one important limitation for adopting the X-ray-selected clusters is that due to the small area coverage in the X-ray surveys (only a small fraction of HSC survey footprint has deep X-ray data for detecting clusters out to high redshifts), the clusters are typically much poorer than those used in our default mock set (see Figure 17), which makes our galaxy selection process more vulnerable to contamination from foreground/background galaxies and may lead to lower completeness. In the future we should use X-ray or SZ selected clusters in order to avoid any selection bias of optically selected clusters which by definition contains prominent concentrations of red cluster member galaxies.

After all the halos in the lightcone patch have been populated with galaxies from real galactic systems (modulo shifts in redshift using passive evolution), we finally remove those galaxies lying in the gap and bright star regions seen in the field galaxy catalog mentioned above, and combine the resulting galaxy catalog with the field galaxy catalog. On average, on top of the $\sim 130,000$ galaxies in the field, we add about 7000 cluster galaxies. We show an example of the distribution of mock galaxies in Figure 18. We note that the spatial distribution of our mock galaxy sample contains several vertical stripes of gaps, which are not seen in most of the HSC Wide layer data. Since these stripes are expected to reduce the completeness estimated from these mock galaxy samples, we expect that our mock analysis results presented in Section 6 are conservative.

As our N -body lightcone covers an octant of the sky, we can extract many patches of the mock sky identical in geometry to the COSMOS field, and thus rapidly generate mock catalogs with area of hundreds of square degrees or more, although the spatial distribution of the field galaxies would be repeated and discontinuous if all the patches are combined together. Furthermore, as the same set of large scale structure in COSMOS are repeated in all the mocks, the effects of large scale structure in cluster finding may not be fully captured in

this approach. We do note that, halos found in filamentary structures surrounding massive halos are also populated with galaxies, and therefore in our mocks the projection effects from surrounding large-scale structures are accounted for to some degree. Finally, it should be emphasized that the way we create the cluster galaxies inevitably rely on several assumptions on the redshift evolution of the cluster galaxy population (e.g., the evolution of the halo occupation number and the red galaxy fraction), and thus our mocks should be regarded as a model, which still need to be calibrated against detailed observations of distant clusters (e.g., Hennig et al. 2017). A proper way to obtain completeness and purity from our mocks is thus to generate sets of mocks that cover the ranges of plausible values of model parameters (e.g., c in equation 17, form and normalization of f_{red}), and marginalize over these mocks.

References

- Aihara, H., et al. 2017, arXiv:1702.08449
- Andreon, S., Maughan, B., Trinchieri, G., & Kurk, J. 2009, A&A, 507, 147
- Andreon, S. 2015, A&A, 582, A100
- Andreon, S., & Hum, M. A. 2010, MNRAS, 404, 1922
- Alam, S., et al. 2015, ApJS, 219, 12
- Allen, S. W., Evrard, A. E., & Mantz, A. B. 2011, ARA&A, 49, 409
- Axelrod, T., Kantor, J., Lupton, R. H., & Pierfederici, F. 2010, Proc. SPIE, 7740, 774015
- Bleem, L. E., et al. 2015, ApJS, 216, 20
- Bosch, J., et al. 2017, arXiv:1705.06766
- Bradshaw, E. J., et al. 2013, MNRAS, 433, 194
- Brammer, G. B., van Dokkum, P. G., & Coppi, P. 2008, ApJ, 686, 1503-1513
- Bruzual, G., & Charlot, S. 2003, MNRAS, 344, 1000
- Carretero, J., Castander, F. J., Gaztañaga, E., Crocce, M., & Fosalba, P. 2015, MNRAS, 447, 646
- Clerc, N., et al. 2014, MNRAS, 444, 2723
- Coil, A. L., et al. 2011, ApJ, 741, 8
- Drinkwater, M. J., et al. 2010, MNRAS, 401, 1429
- Ford, J., Hildebrandt, H., Van Waerbeke, L., Erben, T., Laigle, C., Milkeraitis, M., & Morrison, C. B. 2014, MNRAS, 439, 3755
- Ford, J., et al. 2015, MNRAS, 447, 1304
- Gao, L., Navarro, J. F., Cole, S., Frenk, C. S., White, S. D. M., Springel, V., Jenkins, A., & Neto, A. F. 2008, MNRAS, 387, 536
- Garilli, B., et al. 2014, A&A, 562, A23
- George, M. R., et al. 2011, ApJ, 742, 125
- George, M. R., et al. 2012, ApJ, 757, 2
- Gettings, D. P., et al. 2012, ApJL, 759, L23
- Giles, P. A., et al. 2016, A&A, 592, A3
- Gladders, M. D., & Yee, H. K. C. 2000, AJ, 120, 2148
- Gladders, M. D., & Yee, H. K. C. 2005, ApJS, 157, 1
- Goto, T., et al. 2008, PASJ, 60, S531
- Hansen, S. M., Sheldon, E. S., Wechsler, R. H., & Koester, B. P. 2009, ApJ, 699, 1333
- Hao, J., et al. 2010, ApJS, 191, 254
- Hennig, C., et al. 2017, MNRAS, in press (arXiv:1604.00988)
- Ivezic, Z., et al. 2008, arXiv:0805.2366
- Jimeno, P., Broadhurst, T., Lazkoz, R., Angulo, R., Diego, J.-M., Umetsu, K., & Chu, M. 2017, MNRAS, 466, 2658
- Jurić, M., et al. 2015, arXiv:1512.07914
- Koester, B. P., et al. 2007, ApJ, 660, 239
- Kravtsov, A. V., & Borgani, S. 2012, ARA&A, 50, 353
- Le Fèvre, O., et al. 2013, A&A, 559, A14
- Licitra, R., Mei, S., Raichoor, A., Erben, T., & Hildebrandt, H. 2016, MNRAS, 455, 3020
- Lieu, M., et al. 2016, A&A, 592, A4
- Lilly, S. J., et al. 2009, ApJS, 184, 218
- Lin, Y.-T., Mohr, J. J., & Stanford, S. A. 2004, ApJ, 610, 745
- Lin, Y.-T., Mohr, J. J., Gonzalez, A. H., & Stanford, S. A. 2006, ApJL, 650, L99
- Liske, J., et al. 2015, MNRAS, 452, 2087
- Magnier, E. A., et al. 2013, ApJS, 205, 20
- Mahdavi, A., Hoekstra, H., Babul, A., Bildfell, C., Jeltema, T., & Henry, J. P. 2013, ApJ, 767, 116
- McLure, R. J., et al. 2013, MNRAS, 428, 1088
- Mehrtens, N., et al. 2012, MNRAS, 423, 1024
- Milkeraitis, M., van Waerbeke, L., Heymans, C., Hildebrandt, H., Dietrich, J. P., & Erben, T. 2010, MNRAS, 406, 673
- Miyatake, H., et al. 2016, Phys. Rev. Lett., 116, 041301
- Miyazaki, S., et al. 2012, Proc. SPIE, 8446, 84460Z
- Miyazaki, S., et al. 2015, ApJ, 807, 22
- Momcheva, I. G., et al. 2016, ApJS, 225, 27
- Navarro, J. F., Frenk, C. S., & White, S. D. M. 1997, ApJ, 490, 493
- Newman, J. A., et al. 2013, ApJS, 208, 5
- Niemack, M. D., et al. 2010, Proc. SPIE, 7741, 77411S
- Niikura, H., Takada, M., Okabe, N., Martino, R., & Takahashi, R. 2015, PASJ, 67, 103
- Okabe, N., Takada, M., Umetsu, K., Futamase, T., & Smith, G. P. 2010, PASJ, 62, 811
- Okabe, N., Smith, G. P., Umetsu, K., Takada, M., & Futamase, T. 2013, ApJL, 769, L35
- Oguri, M. 2014, MNRAS, 444, 147
- Oguri, M., & Takada, M. 2011, Phys. Rev. D, 83, 023008
- Oguri, M., Takada, M., Okabe, N., & Smith, G. P. 2010, MNRAS, 405, 2215
- Oguri, M., Bayliss, M. B., Dahle, H., Sharon, K., Gladders, M. D., Natarajan, P., Hennawi, J. F., & Koester, B. P. 2012, MNRAS, 420, 3213
- Pacaud, F., et al. 2016, A&A, 592, A2
- Pierre, M., et al. 2004, JCAP, 9, 011
- Pierre, M., et al. 2016, A&A, 592, A1
- Pompei, E., et al. 2016, A&A, 592, A6
- Renzini, A. 2006, ARA&A, 44, 141
- Rettura, A., et al. 2014, ApJ, 797, 109
- Rozo, E., & Rykoff, E. S. 2014, ApJ, 783, 80
- Rozo, E., Evrard, A. E., Rykoff, E. S., & Bartlett, J. G. 2014, MNRAS, 438, 62
- Rykoff, E. S., et al. 2012, ApJ, 746, 178
- Rykoff, E. S., et al. 2014, ApJ, 785, 104
- Rykoff, E. S., et al. 2016, ApJS, 224, 1
- Saro, A., et al. 2015, MNRAS, 454, 2305
- Schlafly, E. F., et al. 2012, ApJ, 756, 158
- Schlegel, D. J., Finkbeiner, D. P., & Davis, M. 1998, ApJ, 500, 525
- Scoville, N., et al. 2007, ApJS, 172, 1
- Sehgal, N., et al. 2010, ApJ, 709, 920

- Sehgal, N., et al. 2013, ApJ, 767, 38
- Sifón, C., et al. 2013, ApJ, 772, 25
- Silverman, J. D., et al. 2015, ApJS, 220, 12
- Song, J., et al. 2012, ApJ, 761, 22
- Sunyaev, R. A., & Zeldovich, Y. B. 1972, Comments on Astrophysics and Space Physics, 4, 173
- Szabo, T., Pierpaoli, E., Dong, F., Pipino, A., & Gunn, J. 2011, ApJ, 736, 21
- Tinker, J., et al. 2008, ApJ, 688, 709
- Tonry, J. L., et al. 2012, ApJ, 750, 99
- Umetsu, K., Broadhurst, T., Zitrin, A., Medezinski, E., Coe, D., & Postman, M. 2011, ApJ, 738, 41
- Umetsu, K., Zitrin, A., Gruen, D., Merten, J., Donahue, M., & Postman, M. 2016, ApJ, 821, 116
- van Uitert, E., et al. 2016, A&A, 586, A43
- Viola, M., et al. 2015, MNRAS, 452, 3529
- Weinberg, D. H., Mortonson, M. J., Eisenstein, D. J., Hirata, C., Riess, A. G., & Rozo, E. 2013, Phys. Rep., 530, 87
- Wen, Z. L., Han, J. L., & Liu, F. S. 2012, ApJS, 199, 34
- Wen, Z. L., & Han, J. L. 2015, ApJ, 807, 178
- Wilson, G., et al. 2009, ApJ, 698, 1943
- Zacharias, N., Monet, D. G., Levine, S. E., Urban, S. E., Gaume, R., & Wycoff, G. L. 2005, VizieR Online Data Catalog, 1297